Supporting Information for

Phototropic growth control of nanoscale pattern formation in photoelectrodeposited Se–Te films

Authors: Bryce Sadtler, Stanley P. Burgos, Nicolas A. Batara, Joseph A. Beardslee, Harry A. Atwater, Nathan S. Lewis

Text S1. Materials and Methods:

Materials. All materials were used as received without further purification. Gallium powder (Ga, 99.999% metals basis), cadmium sulfate 8/3-hydrate ($CdSO_4 \bullet 2.67\ H_2O$, ≥ 99+%), zinc sulfate monohydrate ($ZnSO_4 \bullet 1\ H_2O$, ≥ 99+%), tellurium (IV) oxide (TeO_2, 99+%), and platinum gauze (Pt, 100 mesh, 99.9% metals basis) were purchased from Sigma-Aldrich. Indium shot (In, 99.999% metals basis), selenium (IV) oxide (SeO_2, 99.4% metals basis), and Pt wire (0.5 mm diameter, 99.997% metals basis) were purchased from Alfa Aesar. Acetone (99.9%, ACS grade) and concentrated hydrochloric acid (HCl, ACS grade) were purchased from VWR. Buffered fluoride-bifluoride hydrofluoric acid was purchased from Transene (Buffer HF Improved). High purity, conductive silver (Ag) paint was purchased from Structure Probe Inc. (SPI) supplies. Double-coated conductive carbon and copper tape were purchased from Ted Pella. Loctite Hysol 9460 epoxy adhesive was purchased from McMaster Carr.

Electrode preparation. Single crystal, n-type silicon wafers with the (111) orientation and doped with arsenic were purchased from Addison Engineering Inc. The wafers had a diameter of 125 mm, a thickness of 400 ± 15 μm, and an average resistivity between 0.004 and 0.006 Ω•cm. Single crystal, p-type silicon wafers with the (100) orientation and doped with boron were purchased from Silicon Quest International. The wafers had a diameter of 4 inches, a thickness between 500 and 550 μm, and an average resistivity between 7 and 9 Ω•cm. Gold (Au) substrates were prepared by depositing 100 nm of 99.999% Au via electron beam evaporation onto a quartz slide using a Temescal

BJD 1800 vacuum deposition system from Technical Engineering Services, Inc. Highly oriented pyrolytic graphite (HOPG, Grade SPI-2) was purchased from SPI supplies. These four types of substrates were used as working electrodes to electrodeposit Se–Te films and are referred to as n+Si(111), pSi(100), Au, and HOPG throughout the rest of the Supporting Information.

For Si substrates, the wafer was cleaved into rectangular pieces with areas between 0.8 and 1.8 cm^2. A Ga–In liquid eutectic alloy was prepared by pulverizing the two metals together in a 75:25 weight ratio. Ohmic contact was made to the back of the Si wafer by scratching the Ga–In eutectic into the unpolished side of the wafer. A coiled tinned copper (Sn–Cu) wire was attached to back of the Si substrate with Ga–In eutectic and coated with conductive Ag paint to seal the wire onto the substrate. The wire was then threaded through a glass tube such that the surface-normal direction of the Si substrate was perpendicular to the glass tube. Hysol 9460 epoxy was used to seal the opening of the glass tube. The epoxy was allowed to dry in air for at least one hour before placing in a drying oven at 65°C for one hour. Nail polish was then used to cover the sides and back of the Si substrate such that electrodeposition of the Se–Te film occurred only on the polished, front side of the electrode.

For Au electrodes, a Sn–Cu wire was made into a ring around the perimeter of the front side of the substrate and attached to the Au surface using Ag paint. The rest of the wire was threaded through a glass tube as described above. The exposed wire and Ag paint on the substrate were covered with nail polish. For HOPG electrodes, a layer of graphite was peeled from the HOPG substrate and affixed onto a fluorine doped tin oxide (FTO) glass substrate using carbon tape. Electrical contact was made to the HOPG layer in a similar way as for the Au substrates. The Au and HOPG electrodes had approximate areas of 0.5 cm^2

Immediately before use, each electrode was rinsed with 18.3 MΩ•cm resistivity H_2O from a Barnsted Nanopure water purification system and dried under a stream of nitrogen gas. The electrode was then briefly exposed to concentrated HCl by placing a drop of the acid on the electrode and letting it spread to cover the electrode surface. The nail polish surrounding the sides of the electrode prevented the drop of acid from

spreading past the edge of the exposed electrode surface. To remove the surface oxide on Si substrates, the electrodes were additionally exposed to buffered HF using a similar procedure as for HCl. After each acid exposure the electrode was rinsed with 18.3 MΩ•cm resistivity H_2O and dried under a stream of nitrogen gas.

Photoelectrodeposition of Se–Te films. A Solartron Analytical potentiostat (Model 1287) was used to electrodeposit the Se-Te films using a three-electrode configuration. An Accumet glass-body standard calomel reference electrode (SCE) from Fisher Scientific was used to reference the potential applied to the working electrode via the potentiostat. A glass adapter was fitted around the SCE, which possessed a male 14/20 ground glass joint and ended in a glass tube. A Vycor frit was connected to the glass tube using heat shrink tubing. The counter electrode consisted of a piece of Pt gauze with approximate dimensions of 2 by 1.5 cm. A Pt wire was threaded through the gauze and soldered to a Sn–Cu wire. The Sn–Cu wire was then threaded through a glass tube and sealed with epoxy as described above. The cylindrical electrochemical cell had three female 14/20 ground glass joints to hold the counter, working, and reference electrodes. One side of the cell possessed a flat glass window such that the working electrode could be illuminated during electrodeposition.

The Se–Te films were electrodeposited under cathodic bias from aqueous solutions that contained 20 mM SeO_2, 10 mM TeO_2, 2 M H_2SO_4, and 0.2 M of $CdSO_4$. The addition of 0.2 M $CdSO_4$ to the deposition solution was found to improve both film adhesion and film quality as compared to 0.2 M $ZnSO_4$ or deposition without a metal sulfate. Fig. S7 shows that $CdSO_4$ is not a necessary ingredient to produce the lamellar patterns formed under illumination, which are apparent both when $CdSO_4$ was replaced with $ZnSO_4$ or when no metal sulfate was added. When the deposition solution contained 0.2 M $CdSO_4$, films that were deposited at more negative potentials (e.g. at E = -0.80 V vs. SCE) showed presence of Cd only near the interface between the Se–Te film and the Si substrate as measured by x-ray photoelectron spectroscopy (Fig. S3).

Low resistivity, single crystal Si substrates that were n-type with a (111) orientation were typically used as the working electrode to deposit the Se–Te films. Si substrates that were p-type with a (100) orientation, evaporated Au films, and cleaved

layers of HOPG, were also used as working electrodes, with similar results obtained on all substrates (Fig. S8). The potential, *E*, between the working and reference electrodes was typically held constant at *E* = -0.40, -0.60, or -0.80 V vs. SCE during deposition of the Se–Te films. Cyclic potential sweeps, linear potential sweeps, and square wave potentials were also used to electrodeposit films with similar results obtained for these different potential waveforms (see Table S1).

High power, light-emitting diodes (LEDs) were used to illuminate the working electrode during growth of the Se–Te films. LEDs with wavelengths of 365, 405, 455, 530, 625, 780, and 940 nm were purchased from Thor Labs. The LED illumination was passed through a 30 mm diameter, aspheric condenser lens (Thor, ACL3026) and a mounted Glan–Thompson calcite polarizer (Thor, GTH10M). The distance between the LED and the electrochemical cell were typically adjusted such that the beam diameter overfilled the area of the working electrode. The calcite polarizer was mounted in a rotation holder to rotate the polarization direction of the incident light. In some cases the glass tube of the working electrode was also mounted in a rotation holder to vary the angle of the incident light. An ELH halogen light bulb and a 633 nm He–Ne laser were also used as illumination sources. A 10× beam expander (Melle–Griot) was used to spread the beam of the He–Ne laser.

A calibrated Si photodiode (Thor, FDS 100–CAL) was used to measure the incident light intensity. Sn–Cu wires were soldered to the leads of the photodiode. The wires were threaded through a glass rod, which was sealed to the photodiode with epoxy in a similar manner as described above. The surface normal of the photodiode was oriented perpendicular to the glass tube. Before each run, the photodiode was placed in the electrochemical cell at the same position where the working electrode would be placed during film growth. The incident light intensity was measured, and the photodiode was removed and then replaced with the working electrode.

The specific conditions used to electrodeposit each sample are provided in Tables S1 and S2 below. Table S1 lists the type of substrate used as the working electrode, the area of the electrode, and the potential waveform applied during deposition. Table S2 lists the illumination conditions including the wavelength, polarization, incident angle,

and intensity of the light source. The compositions of several samples were measured by energy dispersive spectroscopy and are provided in Table S2.

After film growth each electrode was rinsed with 18.3 MΩ•cm resistivity H_2O and then soaked in acetone. As the nail polish and Ag paint dissolved in the acetone, the substrate detached from the Sn–Cu wire, facilitating characterization of the film as described below. Cross-sections of the Se–Te films were prepared by scribing a line in the back of the Si substrate and then snapping the Si substrate into two pieces over a glass slide.

Table S1. Electrodeposition parameters for Se–Te film growth

Sample #	Sample shown in Figure X	Electrode area (cm^2)	Substrate	Potential wave form	Potential range (V)[a]	Sweep rate (mV/s)[b]	No. potential cycles[b]	Deposition time (s)[c]	Total charge passed (C/cm^2)[c]
1	1A, S2, S3	1.29	n+Si(111)	Constant	-0.80				-1.9
2	1B, S2	1.37	n+Si(111)	Constant	-0.80				-1.9
3	1D	1.84	n+Si(111)	Constant	-0.60				-1.9
4	1D	1.7	n+Si(111)	Constant	-0.80				-1.9
5	2A, S4A	1.29	n+Si(111)	Constant	-0.40			500	
6	2B, S4A	1.26	n+Si(111)	Constant	-0.40			500	
7	2C, S4A	1.15	n+Si(111)	Constant	-0.40			500	
8	2D, S4A	1.10	n+Si(111)	Constant	-0.40			500	
9	2E	1.16	n+Si(111)	Constant	-0.40			1000	
10	2F, S4B	1.20	n+Si(111)	Constant	-0.40			3000	
11	2G	1.34	n+Si(111)	Constant	-0.40				-1.25
12	2H	1.23	n+Si(111)	Constant	-0.60				-1.25
13	2I	1.29	n+Si(111)	Constant	-0.80				-1.25
14	3A	1.08	n+Si(111)	Cyclic sweep	0 to -1.0	20	3		
15	3B	1.07	n+Si(111)	Cyclic sweep	0 to -1.0	20	3		
16	3C	1.03	n+Si(111)	Cyclic sweep	0 to -1.0	20	3		
17, Run 1[d]	3D	0.80	n+Si(111)	Cyclic sweep	0 to -1.0	20	3		
17, Run 2	3D	0.80	n+Si(111)	Cyclic sweep	0 to -1.0	20	3		
18	3E	1.06	n+Si(111)	Square wave	0 V, 3 s -0.75 V, 4 s		110		
19	3F, 4	0.96	n+Si(111)	Constant	-0.40				-1.5
20	3G, 4	1.12	n+Si(111)	Constant	-0.40				-1.5
21	3H, 4	1.19	n+Si(111)	Constant	-0.40				-1.5
22	3I, 4	1.02	n+Si(111)	Constant	-0.40				-1.5
23, Run 1[d]	3J	1.42	n+Si(111)	Constant	-0.40				-1.5
23, Run 2	3J	1.42	n+Si(111)	Constant	-0.40				-1.5
24	3K	1.0	n+Si(111)	Constant	-0.40				-1.3
25	3L	1.12	n+Si(111)	Constant	-0.40				-1.3

Sample #	Sample shown in Figure X	Electrode area (cm^2)	Substrate	Potential wave form	Potential range (V)[a]	Sweep rate (mV/s)[b]	No. potential cycles[b]	Deposition time (s)[c]	Total charge passed (C/cm^2)[c]
26	3M	1.02	n+Si(111)	Constant	-0.40				-1.3
27	3N	1.10	n+Si(111)	Constant	-0.40				-1.3
28, Run 1[d]	3O	1.12	n+Si(111)	Constant	-0.40				-0.9
28, Run 2	3O	1.12	n+Si(111)	Constant	-0.40				-1.1
29	S1A	1.04	n+Si(111)	Constant	-0.40				-1.25
30	S1B	1.16	n+Si(111)	Constant	-0.40				-1.25
31	S1C	1.10	n+Si(111)	Constant	-0.40				-1.25
32	S3	0.98	n+Si(111)	Constant	-0.80				-1.2
33	S3	1.23	n+Si(111)	Constant	-0.40				-1.2
34	4, S6A	1.08	n+Si(111)	Constant	-0.40				-1.5
35	4, S6B	1.23	n+Si(111)	Constant	-0.40				-1.5
36	4, S6C	1.08	n+Si(111)	Constant	-0.40				-1.5
37	S7A, B	1.49	n+Si(111)	Constant	-0.60				-2.5
38	S7C, D	1.40	n+Si(111)	Constant	-0.60				-2.1
39	S7E, F	1.27	n+Si(111)	Constant	-0.60				-2.1
40	S8A	0.51	Au	Linear sweep	0 to -0.75	20	6		
41	S8B	0.49	Au	Linear sweep	0 to -0.75	20	6		
42	S8C	0.44	HOPG	Linear sweep	0 to -0.75	20	6		
43	S8D	0.45	HOPG	Linear sweep	0 to -0.75	20	6		
44	S8E	1.08	n+Si(111)	Cyclic sweep	0 to -1.0	20	5		
45	S8F	1.16	n+Si(111)	Cyclic sweep	0 to -1.0	20	5		
46	S8G	1.54	pSi(100)	Cyclic sweep	0 to -1.0	20	5		

[a] A single potential value is provided for constant potential depositions. The initial and final potentials are provided for cyclic and linear potential sweeps.

[b] For a potential sweep, the sweep rate and number of cycles determined the total deposition time. In a cyclic sweep the potential was swept from the initial to the final value and then swept back to the initial value at the same rate before the next cycle. For a linear sweep, the potential was swept from the initial to the final value and then reset back to the initial potential before the next cycle. For a square wave potential the number of cycles refers to the number of times switched between the two listed potential values.

[c] For potentiostatic depositions, the growth was stopped either after a fixed amount of time or after a fixed amount of charge was passed between the working and counter electrodes.

[d] Run number indicates that deposition was stopped, and the illumination conditions were changed before the deposition was resumed on the same electrode.

Table S2. Illumination conditions for Se–Te film growth

Sample #	Sample shown in Figure X	Illumination wavelength (nm)[a]	Polarization orientation[b]	Angle of incidence (degrees)[b]	Light intensity (mW/cm^2)	Se:Te ratio from EDS
1	1A, S2, S3	Dark	-	-	-	58:42
2	1B, S2	625	Vertical	0	16.9	57:43
3	1D	Dark	-	-	-	56:44
4	1D	625	Vertical	0	18.7	60:40
5	2A, S4A	625	Vertical	0	2.8	-
6	2B, S4A	625	Vertical	0	5.6	54:46
7	2C, S4A	625	Vertical	0	11.3	56:44
8	2D, S4A	625	Vertical	0	18.9	62:38
9	2E	625	Vertical	0	18.7	63:37
10	2F, S4B	625	Vertical	0	18.6	64:36
11	2G	625	Vertical	0	18.6	-
12	2H	625	Vertical	0	18.8	-
13	2I	625	Vertical	0	18.6	-
14	3A	625	Unpolarized	0	14.6	53:47
15	3B	625	45°	0	14.5	49:51
16	3C	625	Horizontal	0	14.7	55:45
17, Run 1	3D	940	Vertical	0	31.0	-
17, Run 2	3D	940	Horizontal	0	31.0	-
18	3E	940	Rotated 5° CCW each cycle, 550° total	0	Did not record	-
19	3F, 4	365	Vertical	0	32.5	55:45
20	3G, 4	530	Vertical	0	14.6	53:47
21	3H, 4	780	Vertical	0	17.2	50:50
22	3I, 4	940	Vertical	0	29.8	57:43
23, Run 1	3J	940	Vertical	0	29.5	-
23, Run 2	3J	455	Vertical	0	29.0	55:45
24	3K	625	Vertical	0	18.8	58:42
25	3L	625	Vertical	20°	19.1	58:42
26	3M	625	Vertical	40°	18.8	58:42
27	3N	625	Vertical	60°	18.8	56:44
28, Run 1	3O	625	Vertical	60°	18.8	-
28, Run 2	3O	625	Vertical	-60°	18.8	62:38
29	S1A	ELH lamp	Unpolarized	0	46.5	56:44
30	S1B	ELH lamp	Vertical	0	44.7	58:42
31	S1C	633 nm He–Ne laser	Vertical	0	20.3	60:40
32	S3	625	Vertical	0	18.9	65:35
33	S3	625	Vertical	0	18.4	63:37
34	4, S6A	405	Vertical	0	23.2	57:43
35	4, S6B	455	Vertical	0	23.0	61:39
36	4, S6C	625	Vertical	0	16.0	52:48
37	S7A, B	625	Vertical	0	18.7	63:37
38	S7C, D	625	Vertical	0	18.7	62:38
39	S7E, F	625	Vertical	0	18.6	62:38
40	S8A	Dark	-	-	-	-
41	S8B	530	Vertical	0	8.9	-
42	S8C	Dark	-	-	-	54:46

Sample #	Sample shown in Figure X	Illumination wavelength (nm)[a]	Polarization orientation[b]	Angle of incidence (degrees)[b]	Light intensity (mW/cm^2)	Se:Te ratio from EDS
43	S8D	530	Vertical	0	10.7	56:44
44	S8E	Dark	-	-	-	47:53
45	S8F	625	Vertical	0	18.6	51:49
46	S8G	530	Vertical	0	12.1	52:48

[a] The illumination source was an LED unless otherwise noted.

[b] All top-down SEM images of the Se–Te films are oriented such that if the substrate was parallel to the plane of the page during growth then the illumination direction would have been normal to the page for a 0° incident angle. A vertical polarization orientation means the electric field vector of the incident light would have been parallel to the long edge of the page. For cross-sectional SEM images, the illumination direction would be in the plane of the page and parallel to the long edge of the page for a 0° incident angle. The polarization direction in cross-sectional images is normal to the plane of the page.

Text S2. Film characterization:

Scanning electron microscopy (SEM) was performed using a Zeiss model 1550VP field-emission scanning electron microscope operated at an acceleration voltage of 2 keV. After the growth substrate was detached from the Sn–Cu wire as described above, the substrate was affixed to the SEM sample chuck using copper tape. A below-lens secondary electron detector was used to image the samples. Energy-dispersive spectroscopy (EDS) was performed at an acceleration voltage of 20 keV using either an Oxford INCA 300 or a X-Max SDD X-ray EDS system. The average height, width, and period of the lamellar features were measured from SEM images using Image-J analysis software. To measure the variation in lamellar peak heights and widths as a function of growth time, 50 measurements were taken for each sample. The average value and 1st standard deviation are reported in the text of the main manuscript. To measure the variation in lamellar period as a function of illumination wavelength, 25 measurements were taken for each sample. The average value and 2nd standard deviation are shown in Fig. 4.

X-ray diffraction (XRD) patterns were obtained using a Bruker D2 Phaser with a Cu radiation source (1.54184 Å) and a Lynxeye line detector. The samples were prepared by scraping the Se–Te films off the Si(111) growth substrate using a tungsten carbide razor blade and transferring the material onto a zero background Si(511) XRD plate. Each sample was scanned from 16º to 80º in 2θ with a step size of 0.06º and an acquisition time of 10 s per step. The samples were rotated at 10 rpm during the measurement. The diffraction peak line widths were analyzed using Diffrac Suite EVA software.

X-ray photoelectron spectroscopy (XPS) depth profiling was performed on a Kratos Axis Ultra system with a base pressure below 1×10^{-9} Torr. An octopole ion gun operating at 3 keV was used to etch through the sample at a rate of ~ 1 nm sec^{-1} in 5 to 10 nm intervals. XPS data were acquired using the 1486.6 eV line from a monochromated Al Kα source at 150 W with a multichannel detector set to a pass energy of 10 eV for the high-resolution scans. Acquisition times were approximately 300 sec per step, depending on the energy region being probed.

To model the complex dielectric function of the Se–Te alloy, spectroscopic ellipsometry was used to measure the complex reflectance ratio, ρ, for p- and s-polarized light given by:

$$\rho = \frac{r_p}{r_s} = \tan\Psi e^{i\Delta} \qquad (1)$$

In equation 1, Ψ is the amplitude ratio and Δ is the phase difference for p-polarized, r_p, and s-polarized, r_s, light reflected off the surface of the Se–Te film. A Sentech Instruments SE 850 spectroscopic ellipsometer equipped with a Xe lamp as the UV-Vis source (300-849 nm) and a halogen lamp combined with an FT-IR spectrometer as the NIR source (850-2200 nm) was used for the measurements. The Se–Te film was grown in the dark on a n+Si(111) substrate and had a thickness of 170 nm as measured by cross-sectional SEM. The Ψ and Δ spectra were recorded at angles of 50°, 55°, 60°, 65°, and 70° in a polarizer-sample-analyzer configuration. The model to determine the complex dielectric function of the Se–Te alloy consisted of a 170 nm thick isotropic film

sandwiched between air and a semi-infinite layer of Si(111). Polynomial fitting of the Ψ and Δ spectra was used to calculate values of the refractive index, n, and extinction coefficient, κ, at 1 nm intervals, where the optical constants were made to be continuous over a 50 nm width at each interval.

The n and κ spectra are shown in Fig. S9*A*. The electrodeposited Se–Te films exhibit similar n and κ spectra to those previously measured for Se–Te alloys grown by thermal evaporation (1). The first direct band gap transitions occur at approximately 1.85 eV for selenium and at approximately 0.33 eV for tellurium. The band gap values can vary by as much as 0.12 eV depending on whether the material is amorphous or crystalline (2–4). Alloys of Se and Te have band gap energies between these two values, which vary systematically with the Se:Te ratio (2–4). For the spectra in Fig. S9*A* the extinction coefficient reaches a minimum value of 0.23 at a wavelength of 925 nm (1.3 eV). Structural disorder induced by the addition of Te to Se produces significant tailing of the band edges as well as the formation of localized states within the band gap, which may explain why the extinction coefficient does not go all the way down to zero and begins to increase at longer wavelengths (3, 4).

Text S3. Optical modeling:

Optical model to simulate the wavelength dependence of the lamellar period in photoelectrodeposited Se–Te films. The interference pattern generated by two aligned dipoles on the surface of a flat Se–Te film sandwiched between a Si substrate and a 1.4 index solution was simulated using full-wave finite-difference time-domain (FDTD) simulations. All FDTD simulations were performed using the Lumerical Solutions, Inc. FDTD software package (http://www.lumerical.com/tcad-products/fdtd/). In the simulations the 100 nm thick Se–Te film was modeled using the n and κ data obtained from spectroscopic ellipsometry in the range of 300 to 1000 nm and the electrodeposition solution was modeled as a uniform 1.4 index environment. The dipoles were placed 2 μm apart, and oriented either parallel or perpendicular to the line of separation to simulate their excitation with plane-waves polarized along these directions.

To obtain the interference pattern generated between the dipoles, the dipoles were excited in phase with a broadband pulse, and the steady state coherent superposition of the fields was obtained by Fourier transforming the field response at the Se–Te/solution interface and normalizing it by the Fourier transform of the source. The resulting steady state field profile generated along the line connecting the two dipoles was then fitted with a sinusoid to obtain the peak-to-peak periodicity of the standing wave pattern. The resulting period of the standing wave intensity pattern at the surface of the Se–Te film, p_{surf}, is given by:

$$p_{surf} = \frac{\lambda_0}{2n_{surf}} \quad (2)$$

In equation 2, λ_0 is the free space illumination wavelength and n_{surf} is the effective index at the surface of the Se–Te film. The effective index was found to be slightly larger than the 1.4 index of the solution, consistent with radiation modes supported at the Se–Te/solution interface that are oscillatory in the 1.4 index solution environment and decay exponentially into the higher index of the absorbing Se–Te material.

Although both dipole orientations generate the same period in the resulting field profile, the interference pattern is more pronounced for the parallel-aligned dipoles as there is a higher density of states for the modes supported along this direction based on the complex dielectric function of the Se–Te material. We note that in this model the physical separation of the dipoles only affects the overall position, but not the actual peak-to-peak period of the interference pattern, as the distance between dipoles only adds an overall phase shift to the interference pattern.

Assuming the growth profile of the Se–Te film is proportional to the intensity of the interference pattern, the model for scattering off the surface of a flat Se–Te film matches the experimentally observed lamellar periods at short illumination wavelengths (see Fig. 4 in the main manuscript). However, at longer wavelengths (i.e. > 600 nm) the experimental period deviates towards longer values compared to those simulated by the surface scattering model. The addition of a Bloch mode component to the field profile that is supported by the evolving periodic lamellar structure produced good agreement

between the experimental and simulated periods over the entire wavelength range used to grow the Se–Te films (365 to 940 nm). The relative contributions of the Bloch mode and surface mode to the period were modeled based on the wavelength-dependent penetration depth of the incident light into the Se–Te material.

To understand the contribution from the Bloch scattering mode to the lamellar period, full-wave FDTD simulations were used to visualize the intensity distribution of lamellar structures with various defined periods as a function of illumination wavelength. The intensity distributions for lamellar structures with a 900 nm height, a 205 nm width, and a 410 nm period under plane-wave illumination with wavelengths of 780, 940, and 1200 nm are plotted in Fig. S10. We identify the resonant wavelength of the structure as being 940 nm since this wavelength generates a field intensity maximum near the top of the lamella structure. At this resonant wavelength there are two intensity peaks per unit cell (one on either side of the lamella structure near the top), so the Bloch wave can be treated as being half in the Se–Te lamellae and half in the surrounding solution. Thus, the periodicity of the Bloch wave intensity pattern, p_{Bloch}, is set to be the average of the effective wavelength in the two materials:

$$p_{Bloch} = \frac{1}{2}(\lambda_{SeTe} + \lambda_{soln}) = \frac{\lambda_0}{2}\left(\frac{1}{n_{SeTe}} + \frac{1}{n_{soln}}\right) \quad (3)$$

In equation 3, λ_{SeTe} and n_{SeTe} are the effective wavelength and refractive index, respectively, within the Se–Te material, and λ_{soln} and n_{soln} are the effective wavelength and refractive index, respectively, in the solution. Because the lamellar structures are illuminated from the top, the incident field scatters into both the Se–Te/solution Bloch mode and the surface mode with an efficiency that is proportional to the photonic figure-of-merit, $fom = (n/\kappa)$ of the Se–Te material. The ratio, n/κ, is proportional to the number of field oscillations that occur in the material before decaying to a value of $1/e$. Using this figure-of-merit, the system is dominated by the Se–Te/solution surface mode at wavelengths where the Se–Te material has a high loss (i.e. a low *fom)*. Consistent with this model, the period produced by the dipole scattering model closely matches the experimental lamellar period at short illumination wavelengths, where the *fom* is close to

0 (Fig. 4, red trace). However, at longer illumination wavelengths where the value of the *fom* sharply increases there is an increasing contribution from the Bloch mode to the wave intensity pattern.

The wavelength dependence of the *fom* is shown in Fig. S9*B*. Assuming that the incident light scatters into both modes with equal weight when the *fom* is at a maximum, fom_{max}, within the experimental wavelength range, we set the fractional weights of the Bloch mode, f_{Bloch}, and surface mode, f_{surf}, to:

$$f_{Bloch} = \frac{fom}{2 \times fom_{\max}} \qquad (4)$$

$$f_{surf} = (1 - f_{Bloch}) \qquad (5)$$

The wavelength dependence of f_{Bloch} and f_{surf} are shown in Fig. S9*C*. Using these fractional weights, the effective period of the structure, p_{eff}, is given by the sum of the weighted Bloch and surface wave periodicities,

$$p_{eff} = f_{Bloch} \times p_{Bloch} + f_{surf} \times p_{surf} \qquad (6)$$

This modified scattering model is plotted in Fig. 4 (black trace) and shows good agreement with the experimental period at both short wavelengths (where the loss is high, so the *fom* is low, and the scattered field is dominated by the surface mode index) and at long wavelengths (where the loss is low, so the *fom* is high, and scattering occurs into both the surface and Bloch modes of the periodic structure).

Iterative growth model. To simulate phototropic growth of the Se–Te lamellar patterns, an iterative model was constructed in which the photocarrier generation rate calculated from electromagnetic simulations controlled the probability for mass addition in Monte Carlo simulations of the evolution of the surface. The two-step growth algorithms were performed on a two-dimensional square mesh starting on a bare silicon substrate. First, the absorbance of the structure under linearly polarized, plane-wave illumination was simulated using FDTD with periodic boundary conditions in the in-plane direction. A planar silicon sheet with a thickness of 3 μm was used for the initial

structure. Matlab was used to perform Monte Carlo simulations where mass was added to the upper surface of the structure with probability, F, based on an Arrhenius constant (equation 7). The absorbance of the new, structured film was then calculated in the same manner as the initial planar film. The absorbance calculation – mass addition process was iterated until the desired cross section was achieved.

$$F(G,N) = \frac{(n_0 + G \times \tau_n)(p_0 + G \times \tau_p)}{n_i^2} \prod_{i=1}^{5} \frac{x_i}{r_i} \quad (7)$$

In equation 7, G is the absorbed power normalized by the photon energy, $h\nu$, n_i is the intrinsic carrier concentration, n_0 is the electron concentration, p_0 is the hole concentration, τ_n is the electron lifetime, τ_p is the hole lifetime, x_i is the fraction of i^{th} nearest neighbors occupied in the square lattice, and r_i is the distance to the i^{th} nearest neighbor. The model assumes Arrhenius kinetics for reductive electron transfer leading to mass addition with the driving force equal to the splitting of the quasi Fermi levels. The multiplicative sum reduces the surface roughness of the film so as to mimic the experimentally observed surface roughness.

For these simulations, the Se–Te films were assumed to be undoped (i.e. $n_0 = p_0 = n_i$) and a value of $n_i = 10^{10}$ cm^{-3} was used for the intrinsic carrier concentration based on previous electrical measurements of Se–Te alloy films (5). A value of 1 μs was used for both the electron and hole carrier lifetimes (6). A two-dimensional square mesh with a lattice constant of 1 nm was used for the simulations. A power flux of 16.5 mW/cm^2 was used for the plane-wave illumination source with the electric field perpendicular to the square mesh.

Text S4. Discussion of Supporting Figures:

Figure S1 shows SEM images of Se–Te films that were grown using different illumination sources. In Fig. S1*A* the lamellar pattern was grown under randomly polarized, broadband, non-coherent illumination from a halogen light bulb. The ELH bulb had a maximum irradiance at approximately 620 nm, and the pattern was similar to

that formed under randomly polarized, 625 nm LED illumination (see Fig. 3*A*). However, when a linear polarizer was placed in front of the halogen light bulb, the lamellae oriented parallel to the polarization direction (Fig. S1*B*) similar to those formed using linearly polarized, 625 nm LED illumination (see Fig. 3*B*). Fig. S1*C* shows that similar lamellar patterns were also formed using coherent and monochromatic 633 nm illumination from a He–Ne laser source. Thus, when the central wavelength and polarization direction were similar, the lamellar patterns resulting from illumination using a halogen light bulb, a LED, and a laser exhibited a similar period and orientation. All other lamellar patterns described both in the main manuscript and in the Supporting Information apart from Fig. S1 were grown using LED illumination.

Figure S2 shows representative energy dispersive spectra, EDS, for the Se–Te films shown in Fig. 1*A*, *B* of the main manuscript. Both films were electrodeposited on n+Si(111) substrates at E = -0.80 V vs. SCE until -1.9 C/cm^2 of charge had passed between the counter and working electrodes. One film was grown in the dark (black trace) and the other under linearly polarized, 625 nm illumination with an intensity of 16.9 mW/cm^2 (red trace). EDS indicated that the two films were composed of selenium and tellurium with the atomic ratio, Se:Te, equal to 58:42 for the film grown in the dark and 57:43 for the film under illumination. The Se:Te ratios for other samples are provided in Table S2. The composition of the Se–Te films was probed further by XPS, by use of an ion-sputtering gun to remove material while the spectra were recorded as a function of the film depth. Fig. S3*A* shows spectra in the binding energy regions for Te 3d (left graph) and Se 3d (right graph) photoelectron peaks for two Se–Te films grown at E = -0.80 V vs. SCE. One film was grown in the dark (black traces) and the other film was grown under linearly polarized, 625 nm illumination with an intensity of 18.9 mW/cm^2 (red traces). The peak positions are indicative of elemental Se and elemental Te and the relative peak intensities are similar for the two films. Fig. S3*B* shows spectra in the binding energy regions for Cd 3d (left graph) and Si 2p (right graph) photoelectron peaks for the same Se–Te film electrodeposited at E = -0.80 V vs. SCE under illumination (red traces) and another film that was grown under similar illumination conditions but at E = -0.40 V vs. SCE (black traces). The two films possessed a similar bulk composition as measured by EDS (see rows 32 and 33 in Table S2). However, XPS

depth profiling revealed the presence of Cd at the interface between the Se–Te film and the underlying Si substrate only for the film grown at the more negative potential of E = -0.80 V vs. SCE.

Figure S4*A* shows the deposition current density for films grown at E = -0.40 V vs. SCE for 500 s under linearly polarized, 625 nm illumination with intensities of 2.8, 5.6, 11.3, and 18.9 mW/cm^2. SEM images of the films are shown in Fig. 2*A–D* of the main manuscript. Fig. S4*B* shows the deposition current density for the film shown in Fig. 2*F*, which was grown E = -0.40 V vs. SCE for 3000 s under linearly polarized, 625 nm illumination with an intensity of 18.6 mW/cm^2. The current density slowly decreased during electrodeposition at a constant potential due to the increasing resistance drop across the film. Fig. S5*A* shows the current densities for Se–Te electrodeposition on n+Si(111) substrates under chopped illumination at E = -0.40, -0.60, and -0.80 V vs. SCE. In all three traces the illumination was linearly polarized at a wavelength of 625 nm with an intensity between 18.2 and 18.3 mW/cm^2. Fig. S5*B* shows the current density for Se–Te electrodeposition on a Au substrate at E = -0.40 V vs. SCE under chopped illumination that was linearly polarized at a wavelength of 625 nm with an intensity of 16.6 mW/cm^2. Table S3 provides the current densities in the dark and under illumination along with the photocurrent enhancement (i.e. ratio of the current density under illumination to the current density in the dark) for these four samples.

Table S3. Current densities in the dark and under illumination for Se–Te electrodeposition at different applied potentials and on different substrates.

Substrate	Applied potential (V vs. SCE)	Dark current density (mA/cm^2)	Light intensity (mW/cm^2)	Current density under illumination (mA/cm^2)	Photocurrent enhancement ratio
n+Si(111)	-0.40	-0.05	18.2	-1.79	36
n+Si(111)	-0.60	-0.12	18.3	-2.55	21
n+Si(111)	-0.80	-0.48	18.3	-2.62	5
Au	-0.40	-0.88	16.6	-3.42	4

Figure S6 shows SEM images of lamellar patterns grown under linearly polarized illumination with wavelengths of 405, 455, and 625 nm. These three samples along with

the four samples shown in Fig. 3*F–I* were used to measure the lamellar period vs. illumination wavelength shown in Fig. 4.

Figure S7 shows the effect of adding $CdSO_4$ or $ZnSO_4$ at a concentration of 0.2 M to the electrodeposition solution. Phototropic growth of the lamellar patterns was observed in both cases as well as in the case where no metal sulfate was added (see high magnification images in Fig. S7*A*, *C*, *E*). The addition of $CdSO_4$ improved both adhesion of the Se–Te films to the Si substrate as well as the uniformity of the Se–Te films (see low magnification images in Fig. S7*B*, *D*, *F*). Therefore, the deposition solution contained 0.2 M $CdSO_4$ for all other films described in the manuscript. While the presence of Cd was detected by XPS at the interface between the Si substrate and the Se–Te film, analysis by XRD (Fig. 1*D*), EDS (Fig. S2), and XPS (Fig. S3) all indicate that the bulk of the films were composed of an alloy of elemental Se and elemental Te.

Figure S8 shows SEM images of Se–Te films grown on different substrates used as the working electrode during electrodeposition. Electrodeposited Se–Te films grown in the dark on n+Si(111), Au, and HOPG substrates showed a similar granular morphology (Fig. S8*A*, *C*, *E*). Phototropic growth of the lamellar patterns was observed for films grown under illumination on these same substrates as well as for pSi(100) substrates (Fig. S8*B*, *D*, *F*, *G*). The Se–Te films could only be deposited on the photoconductive pSi(100) substrates under illumination due to the high resistivity (7 to 9 Ω•cm) of these substrates in the dark.

Figures S9 and S10 are described in Text S3 above on the optical model to simulate the wavelength dependence of the lamellar period in the Se–Te films.

Supporting References:

1. Adachi H & Kao KC (1980) Dispersive optical constants of amorphous $Se_{1-x}Te_x$ films. *J Appl Phys* 51(12):6326-6331.

2. Beyer W, Mell H, & Stuke J (1971) Conductivity and thermoelectric power of trigonal Se_xTe_{1-x} single crystals. *Phys Stat Sol (b)* 45(1):153-162.

3. Bhatnagar AK, Srivastava V, & Reddy KV (1998) Te substitution in disordered dilute $Se_{1-x}Te_x$ alloys. *Appl Phys Lett* 73(17):2426-2428.

4. Reddy KV & Bhatnagar AK (1992) Electrical and optical studies on amorphous Se–Te alloys. *J Physics D Appl Phys* 25(12):1810-1816.

5. El-Korashy A, El-Zahed H, Zayed HA, & Kenawy MA (1995) Effect of composition and structure on electrical conduction of $Se_{(100-x)}Te_{(x)}$ fims. *Solid State Commun* 95(5):335-339.

6. Mott NF & Davis EA (1971) *Electronic Processes in Non-Crystalline Materials* (Oxford University Press, New York) 2nd English Ed.

Supporting Figures:

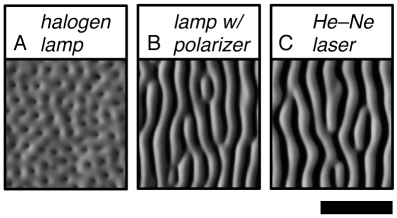

Fig. S1. Photoelectrodeposition of Se–Te films using different illumination sources. (*A*) SEM image of a film grown under randomly polarized illumination from a halogen light bulb with an intensity of 46.5 mW/cm^2. (*B*) SEM image of a lamellar film grown under linearly polarized illumination from a halogen light bulb with an intensity of 44.7 mW/cm^2. (*C*) SEM image of a lamellar film grown under linearly polarized illumination from a 633 nm He–Ne laser with an intensity of 20.3 mW/cm^2. The scale bar is 1 μm and applies to all images.

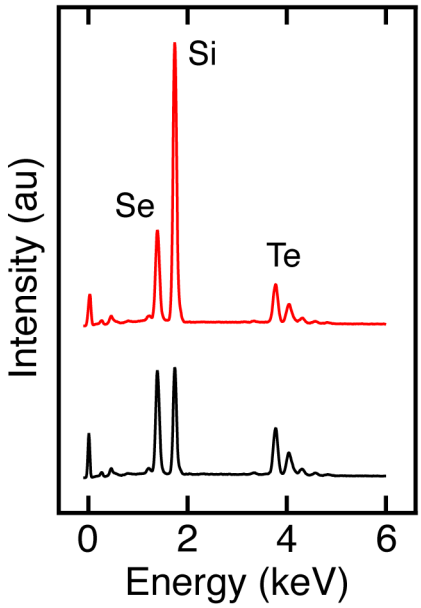

Fig. S2. Energy dispersive spectra of Se–Te films grown in the dark and under illumination. The film grown in the dark (bottom, black trace) possessed an Se:Te atomic ratio of 58:42, while the film grown under illumination (top, red trace) possessed an Se:Te atomic ratio of 57:43. SEM images of the films are shown in Fig. 1*A*, *B* of the main manuscript.

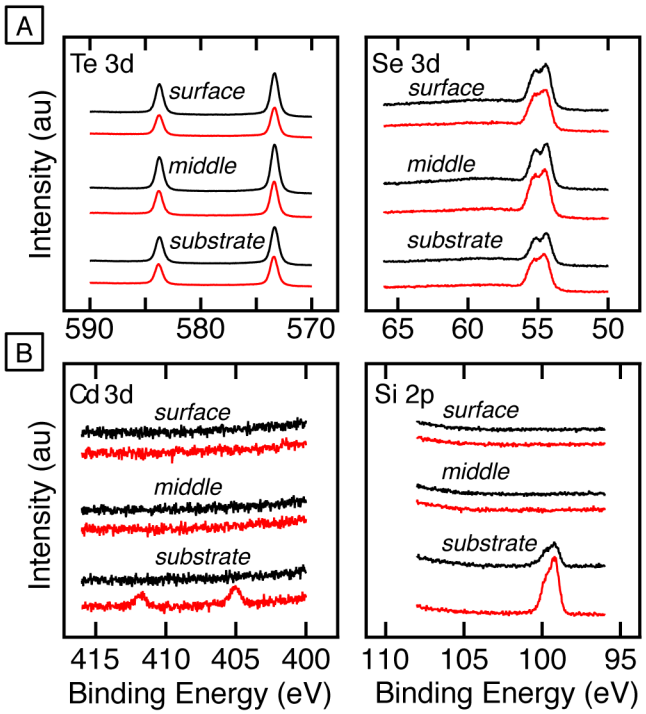

Fig. S3. XPS depth profiling of Se–Te films grown under different illumination and electrochemical conditions. (*A*) Binding energy regions for Te 3d (left graph) and Se 3d (right graph) photoelectron peaks for two Se–Te films grown at a potential of E = -0.80 V vs. SCE in the dark (black traces) and under linearly polarized, 625 nm illumination with an intensity of 18.9 mW/cm^2 (red traces). From top to bottom in both graphs, the spectra were recorded after 30, 150, and 240 seconds of sputtering for the film grown in the dark (black traces) and after 30, 180, and 360 seconds of sputtering for the film grown under illumination (red traces). (*B*) Binding energy regions for Cd 3d (left graph) and Si 2p (right graph) photoelectron peaks for Se–Te films grown under linearly polarized, 625 nm illumination with an intensity of 18.9 mW/cm^2 at E = -0.80 V vs. SCE (red traces) and with an intensity of 18.4 mW/cm^2 at E = -0.40 V vs. SCE (black traces). From top to bottom in both graphs, the spectra were recorded after 30, 180, and 360 seconds of sputtering the film grown at E = -0.80 V vs. SCE (red traces) and after 30, 150, and 300 seconds of sputtering for the film grown at E = -0.40 V vs. SCE (black traces). A Cd signal was only observed for the film grown at E = -0.80 V vs. SCE at the interface with the Si substrate.

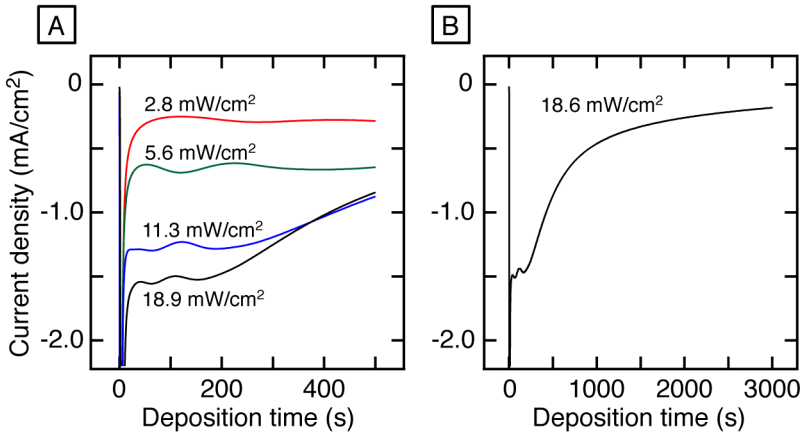

Fig. S4. Current density during potentiostatic photoelectrodeposition of Se–Te films. (*A*) Plots of current density vs. deposition time for Se–Te films grown at E = -0.40 V vs. SCE for 500 s under linearly polarized, 625 nm light with intensities of 2.8, 5.6, 11.3, and 18.9 mW/cm^2. SEM images for these films are shown in Fig. 2*A–D*. (*B*) Plot of current density vs. deposition time for an Se–Te film grown at E = -0.40 V vs. SCE for 3000 s under linearly polarized, 625 nm light with an intensity of 18.6 mW/cm^2. An SEM image of this film is shown in Fig. 2*F*.

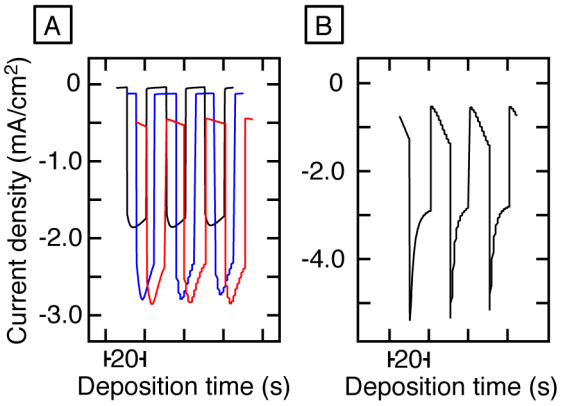

Fig. S5. Current density for Se–Te electrodeposition under chopped illumination at different applied potentials and using different growth substrates. (*A*) Films grown on n+Si(111) substrates under chopped, linearly polarized, 625 nm with an intensity between 18.2 and 18.3 mW/cm^2 at E = -0.40 V (left, black trace), -0.60 V (middle, blue trace), and -0.80 V (right, red trace) vs. SCE. The traces have been offset in time for clarity. (*B*) Film grown on a Au substrate under chopped, linearly polarized, 625 nm with an intensity of 16.6 mW/cm^2 at E = -0.40 V. The average current densities in the dark and under illumination and the photocurrent enhancement ratio for these traces are provided in Table S3.

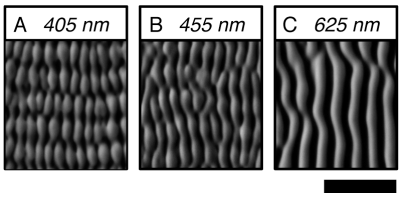

Fig. S6. Wavelength dependence of lamellar period continued from Fig. 3. SEM images of lamellar patterns grown under linearly polarized illumination with wavelengths of (*A*) 405 nm, (*B*) 455 nm, and (*C*) 625 nm. These three samples along with the four shown in Fig. 3*F–I* were used to plot the lamellar period vs. illumination wavelength shown in Fig. 4. The scale bar is 1 μm and applies to all images.

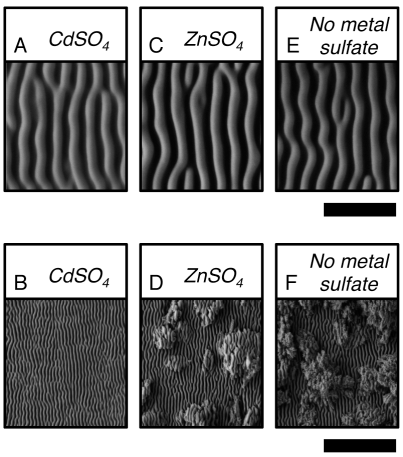

Fig. S7. Photoelectrodeposition of Se–Te films with different metal sulfates added to the deposition solution. All deposition solutions contained 20 mM SeO_2, 10 mM TeO_2, and 2 M H_2SO_4. All films were electrodeposited at E = -0.60 V vs. SCE under linearly polarized, 625 nm illumination with an intensity between 18.6 and 18.7 mW/cm^2. (*A*) High magnification and (*B*) low magnification SEM images of a film grown using a deposition solution that also contained 0.2 M $CdSO_4$. (*C*) High magnification and (*D*) low magnification SEM images of a film grown using a deposition solution that also contained 0.2 M $ZnSO_4$. (*E*) High magnification and (*F*) low magnification SEM images of a film grown using a deposition solution that did not contain a metal sulfate. The scale bar is 1 μm for the top row of images (*A*, *C*, *E*) and 5 μm for the bottom row of images (*B*, *D*, *F*).

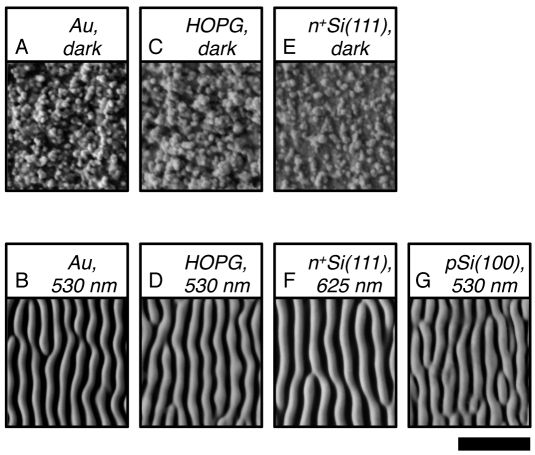

Fig. S8. Electrodeposition of Se–Te films on different substrates in the dark and under illumination. (*A*) Dark electrodeposition of Se–Te on an evaporated Au film. (*B*) Electrodeposition on an evaporated Au film under linearly polarized, 530 nm illumination with an intensity of 8.9 mW/cm^2. (*C*) Dark electrodeposition of Se–Te on a HOPG film. (*D*) Electrodeposition on HOPG under linearly polarized, 530 nm illumination with an intensity of 10.7 mW/cm^2. (*E*) Dark electrodeposition of Se–Te on a n+Si(111) substrate. (*F*) Electrodeposition on n+Si(111) under linearly polarized, 625 nm illumination with an intensity of 18.6 mW/cm^2. (*G*) Electrodeposition of Se–Te on pSi(100) under linearly polarized, 530 nm illumination with an intensity of 12.1 mW/cm^2. The scale bar is 1 μm and applies to all images.

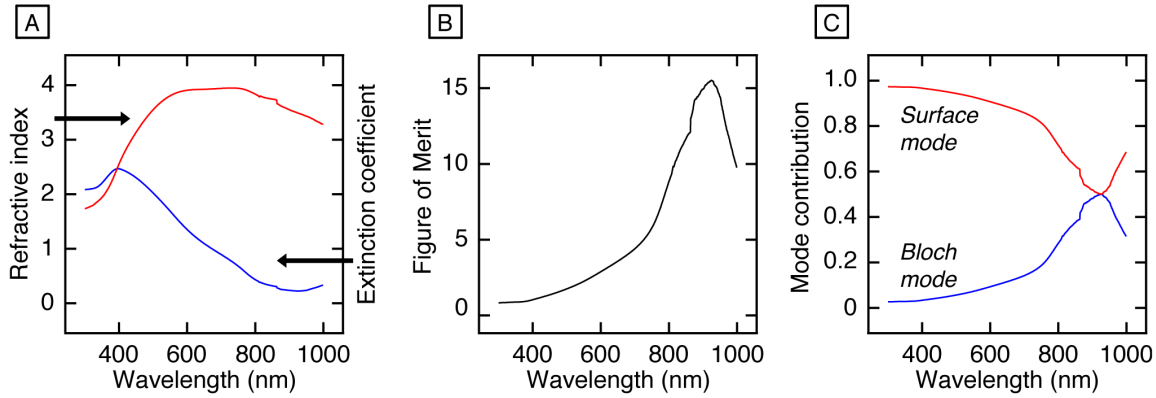

Fig. S9. Optical modeling used to simulate the lamellar period as a function of illumination wavelength. (*A*) Refractive index, n, and extinction coefficient, κ, for the Se–Te alloy modeled from spectroscopic ellipsometry measurements. The discontinuity in the spectra at 850 nm is due to the change in illumination source. (*B*) Photonic figure of merit, $fom = n/\kappa$, used to model the contribution of the surface and Bloch modes to the scattered intensity profile. (*C*) The relative contributions for the surface and Bloch modes, which were assumed to be equal when the *fom* was at a maximum.

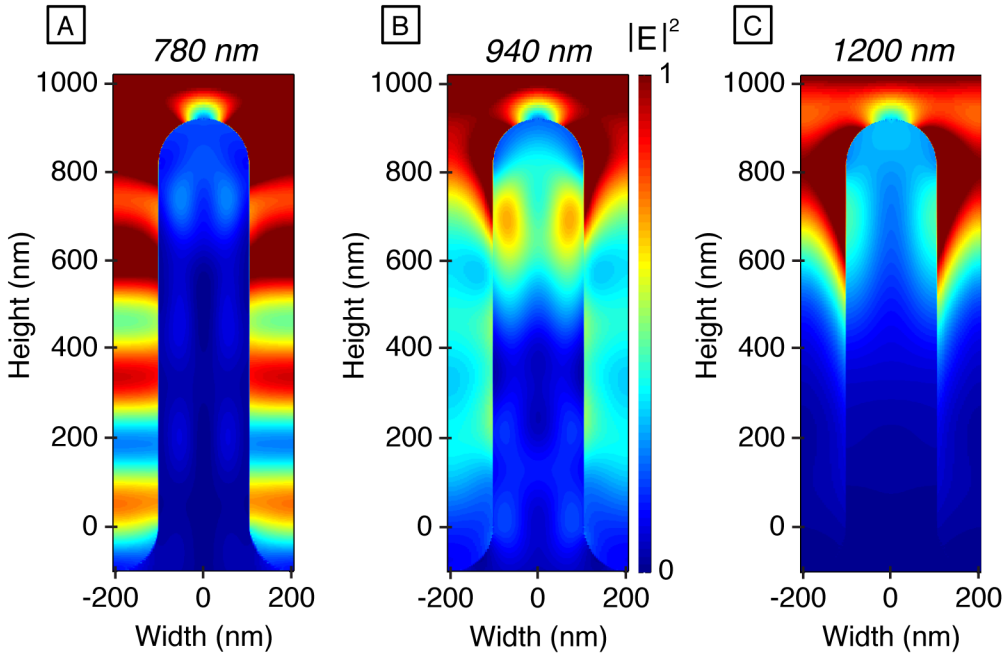

Fig. S10. FDTD simulations of the intensity profile for periodic Se–Te structures under plane-wave illumination. The lamellar structures were constructed with a 900 nm height, a 205 nm width, and a 410 nm period. The images show one unit cell, and periodic boundary conditions were used for the simulations. The intensity distributions are shown for the structures under plane-wave illumination with wavelengths of (*A*) 780 nm, (*B*) 940 nm, and (*C*) 1200 nm. The intensity scale, $|E|^2$, shown in *B* applies to all three images.